Evaluation and optimization of mass transport of redox species in silicon microwire-array photoelectrodes

Chengxiang Xiang[1], Andrew C. Meng[1], and Nathan S. Lewis[2]

Beckman Institute and Kavli Nanoscience Institute, Division of Chemistry and Chemical Engineering, 210 Noyes Laboratory, MC 127-72, California Institute of Technology, Pasadena, CA 91125

Edited by Thomas J. Meyer, University of North Carolina at Chapel Hill, Chapel Hill, NC, and approved July 23, 2012 (received for review December 14, 2011)

Physical integration of a Ag electrical contact internally into a metal/substrate/microstructured Si wire array/oxide/Ag/electrolyte photoelectrochemical solar cell has produced structures that display relatively low ohmic resistance losses, as well as highly efficient mass transport of redox species in the absence of forced convection. Even with front-side illumination, such wire-array based photoelectrochemical solar cells do not require a transparent conducting oxide top contact. In contact with a test electrolyte that contained 50 mM/5.0 mM of the cobaltocenium$^{+/0}$ redox species in CH_3CN–1.0 M $LiClO_4$, when the counterelectrode was placed in the solution and separated from the photoelectrode, mass transport restrictions of redox species in the internal volume of the Si wire array photoelectrode produced low fill factors and limited the obtainable current densities to 17.6 mA cm^{-2} even under high illumination. In contrast, when the physically integrated internal Ag film served as the counter electrode, the redox couple species were regenerated inside the internal volume of the photoelectrode, especially in regions where depletion of the redox species due to mass transport limitations would have otherwise occurred. This behavior allowed the integrated assembly to operate as a two-terminal, stand-alone, photoelectrochemical solar cell. The current density vs. voltage behavior of the integrated photoelectrochemical solar cell produced short-circuit current densities in excess of 80 mA cm^{-2} at high light intensities, and resulted in relatively low losses due to concentration overpotentials at 1 Sun illumination. The integrated wire array-based device architecture also provides design guidance for tandem photoelectrochemical cells for solar-driven water splitting.

semiconductor/liquid junctions | Si microwire arrays | COMSOL Multiphysics

To yield optimal solar energy-conversion efficiencies, photoelectrochemical cells require highly effective mass transport of redox species between the photoelectrode and the counter electrode, as well as in the internal void volume of porous, microstructured photoelectrodes. Although the fundamental energy-conversion properties of many semiconductor photoelectrodes are well-documented, the mass transport of reactants and products in highly structured electrochemical systems has received relatively little attention. Diffusion-limited mass transport during the electrochemical deposition of metals onto planar electrodes has been investigated by Scharifker and Hills (1) in the early 1980s, and has been further expanded upon in other studies (2–5). Penner et al. (6) have studied the mass-transport properties of conical and hemispherical ultramicroelectrodes in electrochemical cells. Mass transport in nanocrystalline TiO_2-based dye-sensitized solar cells has also been treated theoretically (7–12). Of specific interest herein is the mass transport of redox species in the internal pore volume of highly microstructured electrodes, such as Si wire array photoelectrodes.

High aspect-ratio semiconductor microwire and nanowire array structures have shown promise in liquid junction devices for solar energy-conversion applications (13–18). A key attribute of these wire array structures is the orthogonalization of the directions of light absorption and photogenerated charge-carrier collection (19). However, collection of photogenerated charge carriers will be limited if the solution at the base of the wire arrays, where the path length for the transport of redox couple species from the bulk solution is largest, is depleted of reactant species during photocurrent flow in the device.

For many types of photoelectrodes, forced convection produced by rapid stirring in a three-electrode configuration (20), or effective diffusive transport produced by use of a well-designed two-electrode thin-layer cell configuration (10, 21–23), have been utilized to minimize mass transport losses between the photoelectrode and the counter electrode (Scheme 1 *A* and *B*). However, these approaches do not effectively minimize losses due to restricted mass transport in the internal volume of microstructured photoelectrodes, such as Si wire arrays. As part of this work, we have characterized the mass transport limitations of such systems experimentally as well as with finite-element modeling.

The wire-array photoelectrode architecture also offers an intriguing opportunity to produce integrated, two-electrode, photoelectrochemical solar cell structures that could minimize the ohmic resistance and mass transport losses in the external electrolyte solution. Scheme 1*C* depicts an architecture that would provide a stand-alone, two-electrode photoelectrochemical solar cell that would require neither external solution volume nor a transparent conductive top contact. In this architecture, the ohmically contacted substrate provides electrical contact to the photoactive wires, and the counter electrode is a deeply physically embedded metal film that contacts the electrolyte in the internal volume of the photoelectrode, but is separated from the substrate, and from the photoactive microwires, by an electrically insulating barrier layer. By minimizing the distance between the working and counter electrodes, and by not requiring any volume of external solution, this device configuration should produce nearly optimal mass transport of redox species for microstructured photoelectrochemical systems. The ability to generate redox species at the base of the wire array also provides a platform to investigate the mass transport behavior of water-splitting tandem cells in which protons must diffuse from the base of the wire array to reach the photocathode, in order to undergo the reduction reaction needed to complete the fuel production process.

Author contributions: C.X., A.C.M., and N.S.L. designed research; C.X. and A.C.M. performed research; C.X. and A.C.M. analyzed data; and C.X., A.C.M., and N.S.L. wrote the paper.

The authors declare no conflict of interest.

This article is a PNAS Direct Submission.

[1]C.X. and A.C.M. contributed equally to this work.

[2]To whom correspondence should be addressed. E-mail: nslewis@caltech.edu.

This article contains supporting information online at www.pnas.org/lookup/suppl/doi:10.1073/pnas.1118338109/-/DCSupplemental.

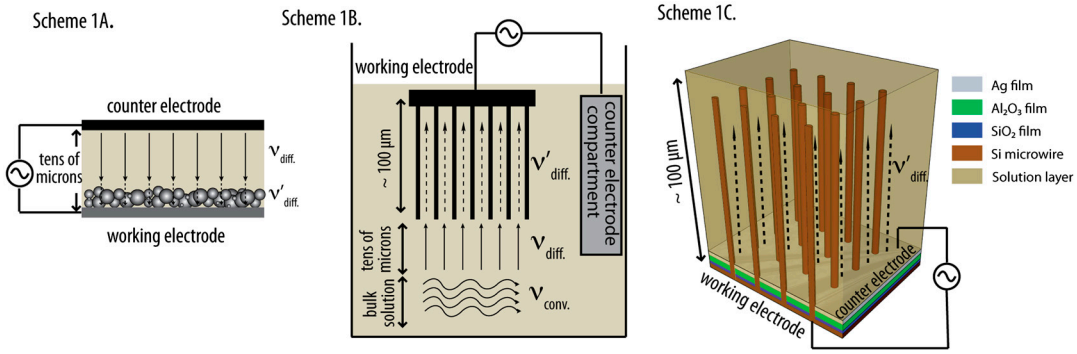

Scheme 1. Schematics of three electrochemical systems that facilitate mass transport between the photoelectrodes and the counter electrodes, where $\upsilon_{conv.}$ illustrates convective mass transport by rapid stirring, $\upsilon_{diff.}$ illustrates diffusive mass transport in solution, and $\upsilon'_{diff.}$ illustrates diffusive mass transport within microporous photoelectrodes. Scheme 1*A* depicts a two-electrode thin-layer configuration that exploits effective diffusive transport. Scheme 1*B* shows a conventional three-electrode configuration that uses rapid convective stirring. Scheme 1*C* illustrates a stand-alone, two-terminal photoelectrochemical solar cell configuration that uses a deeply embedded Ag film as the counter electrode. The typical direction of illumination was normal to the working electrode.

Results

Structure of the Wire Array Electrodes. Fig. 1*A* displays top- and side-view SEM images of the Si microwire arrays that were grown by the VLS process. Fig. 1*B* displays a photograph of a top-down view of a typical Si wire-array substrate, integrated with a Ag film at the base of the wire array. The darker innermost square is the defined photoactive area of Si microwires with interdigitated Ag films; the bordering silver square is the excess Ag film evaporated on the Si substrate; and the outermost striped edge is the Al_2O_3 layer that had been covered by Kapton tape during the Ag evaporation. Fig. 1*C* shows the SEM images of the Ag film, SiO_2 and Al_2O_3 layers at the base of the photoelectrodes. The different layers were identified by the contrast and texture in the image. The Ag/Ti layer had a distinctly textured surface, which is characteristic of polycrystalline metallic films. The two insulating layers had a darker appearance in the cross section due to charging of the electron beam. The Ag film was electrically insulated from the Si microwire arrays by the SiO_2 and Al_2O_3 layers. The SEM image indicated no physical shorting between the Ag film and the Si microwire arrays. The resistance between the Ag film and the Si microwire arrays was approximately 10–100 kΩ.

Simulations of Mass Transport in Microwire Array Electrodes. Fig. 2*A* shows the results of COMSOL Multiphysics simulations of the concentration profiles of the oxidized species (cobaltocenium) within the wire-array photoelectrode in the control configuration (Scheme 2*A*), for which the Si wire-array electrode served as the working electrode, the Pt gauze electrode served as the counter electrode, and the Pt wire served as reference electrode. The bulk concentrations of $CoCp_2^+$ and $CoCp_2^0$ were set to 50 mM and 5.0 mM, respectively. The diffusion coefficients of the $CoCp_2^+$ and $CoCp_2^0$ in CH_3CN were each taken to be 6.4×10^{-6} $cm^2\,s^{-1}$. The thickness of the hydrodynamic boundary layer was set to 3.5 µm, which corresponded to the rapid stirring condition used experimentally when the magnetic stir bar was rotating at approximately 3,000 rpm close to a planar electrode.

Assuming a uniform current density along the wire-array electrodes and a projected-area current density of 10 mA cm^{-2}, the concentration of $CoCp_2^+$ reached zero at a distance from the tops of the wires equal to approximately 30% of the wire height. In the region of the solution where $[CoCp_2^+] = 0$, the photogenerated charge carriers were forced to recombine, because no oxidized species was present to accept electrons at the wire-array surface. Hence, under these conditions, the photogenerated charge-carrier collection was limited by the mass transport of the redox species in the internal volume of the Si microwire array photoelectrode.

In contrast, Fig. 2*B* shows the simulation results for the concentration profiles of $CoCp_2^+$ within the wire-array photoelectrode in the device configuration (Scheme 2*B*), for which the Si wire-array electrode served as working electrode, the base Ag film served as counter electrode, and the Pt wire served as the reference electrode. The minimum in the concentration of $CoCp_2^+$, at a value of $[CoCp_2^+] = 28$ mM, occurred near the mid-point of Si microwire array. Under these operating conditions, the redox species was not fully depleted at any point in the wire-array region.

Fig. 2*C* shows the simulation results for the electric potential profiles of the wire-array photoelectrodes in the stand-alone, two-electrode, solar cell configuration (Scheme 1*C*). The conductivity of the electrolyte, CH_3CN–1.0 M $LiClO_4$, was set to 5.0 S m^{-1}. Assuming a uniform current density along the wire-array electrode and a projected-area current density of 10 mA cm^{-2}, the maximum electric potential drop, which occurred at the center of the top surface of the wire arrays, due to the solution resistance was less than 2 mV. In contrast, under the same oper-

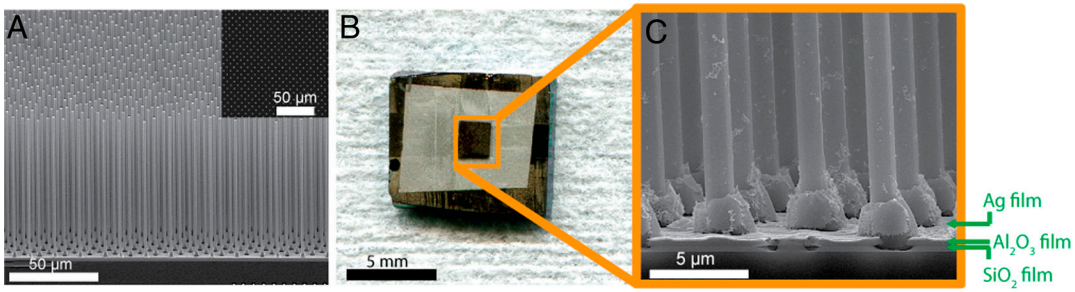

Fig. 1. (*A*) Scanning electron microscope image showing the Si microwire arrays that were grown by VLS process. (*B*) Optical microscopy image showing a typical Si wire-array substrate embedded with a silver film that had been electrically isolated from the wire-array electrode. (*C*) Scanning electron microscope image showing the silver film at the base the electrode, with the Ag electrically insulated from the Si microwire arrays by the Al_2O_3 and SiO_2 isolation layers.

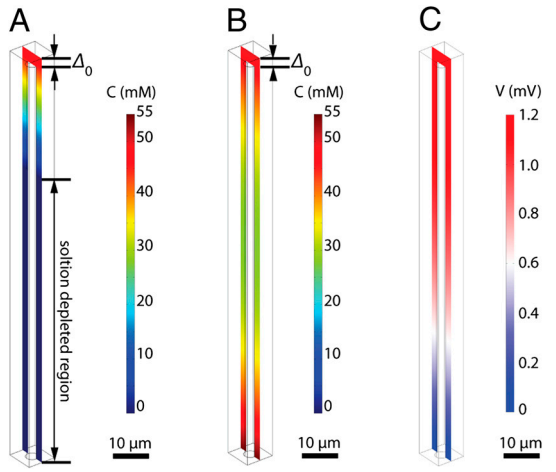

Fig. 2. Finite element simulation (in COMSOL Multiphysics) of the concentration profiles of oxidized species in operating Si microwire photoelectrodes (*A*) in the control configuration and (*B*) in the device configuration, where Δ_0 denotes the hydrodynamic boundary layer thickness. (*C*) Simulation of the electric potential profiles of the wire-array photoelectrodes in the stand-alone, two-electrode configuration (Scheme 1*C*).

ating conditions, the electric potential drop due to the uncompensated resistance in a traditional three-electrode measurement (Scheme 2*A*) was typically approximately 50 mV even when a Luggin capillary reference electrode was used. Hence, the ohmic resistance loss is significantly reduced due to the integrated wire-array architecture of Scheme 1*C*. For comparison, operating at a current density of 10 mA cm^{-2}, a 10 μm thick layer of this electrolyte produces a potential drop of approximately 0.2 mV in a thin-layer configuration between a planar photoelectrode and a planar counterelectrode.

Behavior of Wire Array-Based Photoelectrodes. Fig. 3 compares the *J-E* behavior in contact with CH_3CN–1.0 M $LiClO_4$–0.050 M $CoCp_2^+$–0.0050 M $CoCp_2^0$ of the control configuration (black and green traces) with that of the device configuration (blue and red traces) for Si wire-array electrodes that contained Ag films. In the control configuration (Scheme 2*A*), the Si wire-array electrodes served as the working electrode, the Pt wire served as the reference electrode, and the Pt gauze electrode served as the counter electrode. In the device configuration (Scheme 2*B*), the counter electrode was switched from the Pt gauze electrode to the Ag film so that the redox species were regenerated at the base of the photoelectrode. In the absence of stirring, the *J-E* characteristics of photoelectrodes in the control configuration exhibited large hysteresis due to the limited mass transport within the microwire arrays. Thus, the mass transport limitations of the redox species significantly lowered the photoelectrochemical performance of the photoelectrodes. In contrast, the *J-E* characteristics of photoelectrodes in the device configuration exhibited nearly no hysteresis, and showed much larger short-circuit current densities and fill factors.

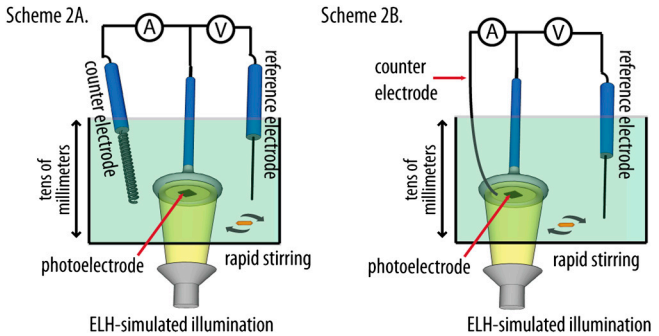

Scheme 2. Schematics of the two photoelectrochemical configurations evaluated in this work. Scheme 2*A* illustrates the control configuration, for which the Si wire-array electrode served as the working electrode, the Pt gauze electrode served as the counter electrode, and the Pt wire served as reference electrode. Scheme 2*B* illustrates the device configuration, for which the Si wire-array electrode served as the working electrode, the Ag film served as the counter electrode, and the Pt wire served as reference electrode. Both configurations employed a W-halogen ELH-type illumination source.

Table 1 summarizes the open-circuit photovoltage, V_{OC}, short-circuit photocurrent density, J_{SC}, and the fill factor, *ff*, values for the two different photoelectrode configurations (Scheme 2 *A* and *B*) under different illumination and stirring conditions. In the absence of forced convection by stirring, at a light intensity equivalent to 4 Suns, the photoelectrodes produced J_{sc} values that were 2.5 times higher in the device configuration (Scheme 2*B*) than in the control configuration (Scheme 2*A*). In the presence of rapid stirring, when the magnetic stir bar was rotating close to the photoelectrode at approximately 3,000 rpm, at 1 Sun the two photoelectrode configurations produced mutually similar *J-E* behavior. In contrast, at 4 Suns, a relatively small but significant improvement in the *J-E* behavior was observed for device configuration relative to the control configuration.

Behavior of Wire Array-Based Photoelectrochemical Solar Cells. Fig. 4 shows the effect of illumination intensity on the current density vs voltage (*J-V*) characteristics of Si wire-array photoelectrodes with internal Ag films, when operated in a stand-alone, two-electrode, solar cell configuration (Scheme 1*C*). In the stand-alone two-electrode configuration, a droplet of propylene carbonate (PC)–1.0 M $LiClO_4$–0.150 M $CoCp_2^+$–0.150 M $CoCp_2^0$ was used to make the semiconductor/liquid junctions. The maximum illumination intensity from the W-halogen ELH-type illumination corresponded to 900 mW cm^{-2}, i.e., 9 Sun, with the light intensity attenuated to lower values, such as 100 mW cm^{-2}, using neutral density filters. Propylene carbonate was used as the solvent because its low volatility minimized evaporation of the liquid in the electrochemical device. Under illumination, the short-circuit current density scaled linearly as a function of the light intensity, reaching 89.1 mA cm^{-2} at 9 Sun, with no significant loss due to mass transport (Fig. 4, insert). In the absence of solution, no appreciable shorting current was observed between the Si microwire arrays and the Ag film (Fig. 4, dashed trace).

Discussion

Si Wire-Array Based Solar Cells. The architecture of structured microwire arrays offers a unique opportunity to achieve deep physical integration of the light absorber, the electrolyte, and the electrical contacts in a photoelectrochemical system that optimizes mass transport of redox species and that minimizes losses due to solution resistance, while obviating the need for a transparent conducting material as the top contact in the solar cell device. The device structure easily sustained short-circuit current densities of approximately 50 mA cm^{-2} at 50 mM concentrations of redox species in the solution (Fig. 3). For comparison, a thin-layer cell with an electrolyte spacing of 10 μm and a redox species having a concentration of 50 mM and a diffusion coefficient of 6.4×10^{-6} cm^2 s^{-1} would provide a mass transport limited current density of approximately 30 mA cm^{-2}, whereas a disk electrode rotating at 3,000 rpm would provide a mass-transport-limited current density of approximately 45 mA cm^{-2} at the same concentration of redox-active species in solution, assuming a kinematic viscosity value of 4.5×10^{-3} cm^2 s^{-1} for CH_3CN. In practice, it is desirable to have the mass-transport-limited current densities be significantly larger than the short-circuit photocurrent densities, to minimize mass-transport overpotentials that would decrease the fill factor, and thus the energy-conversion efficiencies, of the photoelectrode when used as a stand-alone, two terminal, photoelectrochemical solar cell (20, 21, 24).

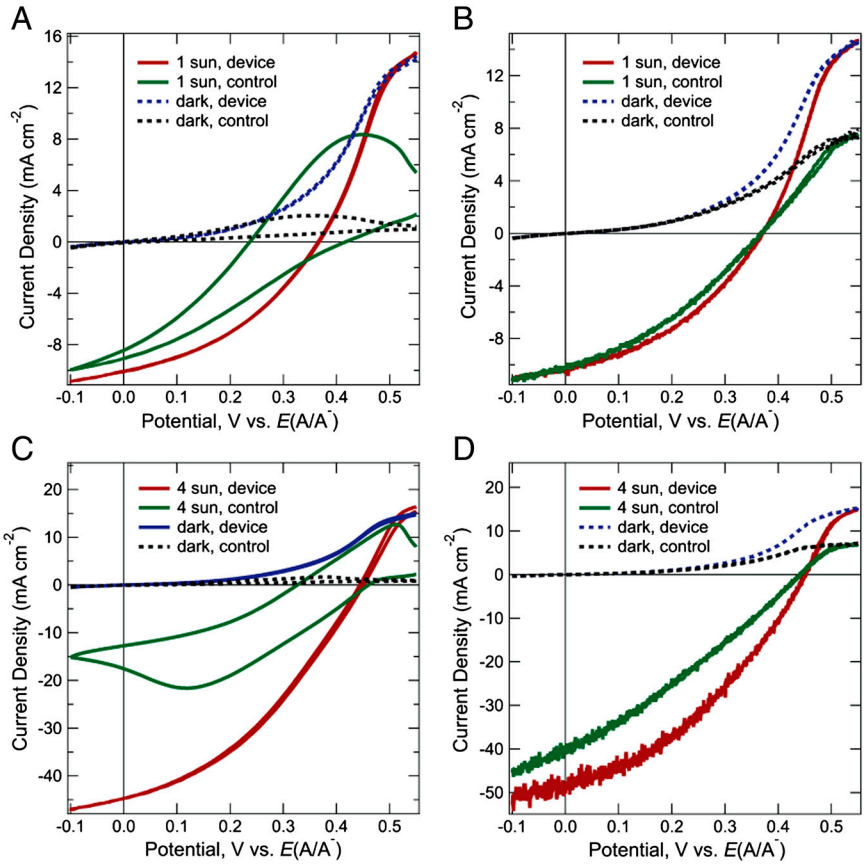

Fig. 3. Current density–potential characteristics of Si wire-array photoelectrodes in the control configuration and in the device configuration. Photoelectrodes were in contact with CH_3CN–1.0 M $LiClO_4$–0.050 M $CoCp_2^+$–0.0050 M $CoCp_2^0$, (*A*) under ELH-simulated 4 sun illumination and without stirring, (*B*) under ELH-simulated 1 sun illumination and with rapid stirring, (*C*) under ELH-simulated 4 sun illumination and without stirring, and (*D*) under ELH-simulated 4 sun illumination and with rapid stirring.

The short-circuit photocurrent density of the wire-array photoelectrode was approximately 10 mA cm^{-2} in the stand-alone, two-electrode configuration under 1 Sun illumination. The observed J_{sc} can be further improved by light trapping techniques (25–28). Using an antireflective coating, a Ag back-reflector and embedded light-scatterers, these wire-array substrates have exhibited up to 96% peak absorption and have been shown to absorb up to 85% of day-integrated, above-bandgap direct-beam sunlight (25). Moreover, the long minority-carrier diffusion length and the low surface recombination velocity of the vapor-liquid-solid (VLS) grown Si microwires has produced broadband, near-unity internal quantum yields for carrier collection through a radial semiconductor/liquid junction (13, 25, 28). The embedded Ag counter-electrode in Scheme 1*C* inherently serves as an effective back-reflector, thereby improving the light absorption in the Si wire-array photoelectrodes. By utilization of an additional antireflective coating and light-scatterers, the energy-conversion efficiency of the Si wire-array photoelectrodes in the stand-alone, two-terminal configuration is expected to be improved significantly. The physical integration of the Ag film in Scheme 1*C* also provides a blueprint for a "wrap-around contact" for a solid-state Si microwire photovoltaic, in which instead of a transparent conducting oxide top contact, the Ag metal layer at the base of the microwire arrays would contact the emitter region of the microwires, thereby providing the "top" contacts to the device.

Mass Transport Effects in Wire Array Photoelectrodes. Most photoelectrochemical cells are designed to allow evaluation of the performance of the semiconductor photoelectrode while minimizing effects that might arise from the electrolyte, such as the series resistance, concentration overpotentials, or optical absorption (20, 29). In contrast, high aspect-ratio Si wire-array photoelectrodes present challenges for mass transport of redox species.

Table 1. Open-circuit voltage, V_{oc}, short-circuit photocurrent density, J_{sc} and fill factor, *ff* data for Si wire-array photoelectrodes in the control configuration and in the device configuration

	V_{OC} (V)			J_{SC} (mA cm^{-2})			*ff*		
Illumination intensity	1 Sun	2 Sun	4 Sun	1 Sun	2 Sun	4 Sun	1 Sun	2 Sun	4 Sun
Device									
No stirring	0.37	0.41	0.45	10.1	20.9	44.7	0.39	0.38	0.38
Rapid stirring	0.37	0.41	0.45	10.4	22.0	48.7	0.38	0.39	0.37
Control									
No stirring*	0.42	0.44	0.46	9.1	16.6	17.6	0.28	0.30	n/a
Rapid stirring	0.37	0.41	0.44	10.2	20.7	40.6	0.35	0.33	0.29

*For the *J-E* behaviors with significant hysteresis, the forward scan results were used to obtain V_{oc}, J_{sc}, and *ff* data.

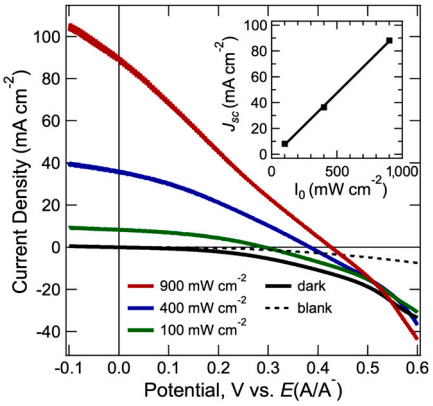

Fig. 4. Illumination intensity dependence of the current density–potential characteristics of Si wire-array photoelectrodes that contained integrated Ag films as a counter electrode in a stand-alone two-electrode configuration in contact with the propylene carbonate–1.0 M $LiClO_4$–0.150 M $CoCp_2^+$–0.150 M $CoCp_2^0$ electrolyte.

Hence, the Ag film counter electrodes that were incorporated at the base of the Si wire-array photoelectrodes reduced the effective diffusive path length of redox species to a value equal to half of the wire-array length, in the case of uniform photogeneration of charge carriers along the length of the wires. Kelzenberg et al. (25, 30) have calculated the photogeneration profiles of 25 μm-long Si microwire arrays using 3D finite-difference time-domain (FDTD) methods. The photogeneration profiles in such systems depend significantly on the incident angle of the illumination source (25). The concentration gradient of redox species in the internal volume of the microwire arrays, and the resulting change in optical absorption along the wire length, further complicate the absorption properties of the Si microwire electrodes. Although a quantitative analysis of light absorption coupled with mass transport is outside the scope of this study, the significant improvement of the short-circuit current densities and fill factors in the absence of stirring, and/or under high illumination intensities (Fig. 3), demonstrated the effectiveness of the fabricated device configuration. Still further improvement of the J-E behavior could be realized by further reductions in the effective ion path length, such as by the use of a p-n$^+$ wire-array electrode, in which photogenerated carriers could travel vertically in the emitter layer along large segments of the wire length.

The increase in the short-circuit current densities for the device configuration relative to the control configuration (Fig. 3) is attributable to the improved mass transport of the redox species, as well as to a reduction at steady-state, in the optical absorption of the redox system in the device configuration. As shown in Table 1, under ELH-simulated 1 Sun illumination and with effective stirring, the short-circuit current densities of the Si wire-array photoelectrodes were nearly identical in the control configuration and the device configuration, indicating negligible reduction of optical absorption of the solution species at the base of the electrode in device configuration at low illumination intensities. Under ELH-simulated 4 Sun illumination and rapid stirring, the Si wire-array photoelectrodes in the device configuration exhibited a J_{sc} value of 48.7 mA cm^{-2}, which was greater than four times the J_{sc} value under 1 Sun illumination, 10.4 mA cm^{-2}. The extra gain of the current density, 7.1 mA cm^{-2} relative to four times the J_{sc} value under 1 Sun, is attributable to reduction of the optical absorption of the solution species, due to the active regeneration in the device configuration of $CoCp_2^+$, which is less absorptive in the visible region than $CoCp_2^0$. The stand-alone two-electrode results exhibited a similar increase in short-circuit current densities relative to the control configuration. The slope of a plot of J_{sc} vs. illumination light intensity (Table 1) increased with increasing light intensity, consistent with expectations for the enhanced depletion of the more absorptive species, $CoCp_2^0$, at the base of the microwire arrays in the device and stand-alone solar cell configurations, relative to the control configuration.

The concentration profiles of $CoCp_2^+$ (Fig. 2) suggest that, due to mass transport limitations, the short-circuit current densities should be significantly reduced in the control configuration because the pores in between the wires were calculated to be depleted of solution species over a distance corresponding to approximately 70% of the length of the wires. However, experiments showed that under 1 Sun illumination and under rapid stirring, the short-circuit current densities in the control configuration were comparable to those of the device configuration (Table 1). This discrepancy between the simulations and the observations can likely be attributed to a non-uniform current density distribution along the length of the microwire array, as well as to the long minority-carrier diffusion length of the p-Si microwire arrays. A long minority-carrier diffusion length (>30 μm), as has been observed in similar p-Si microwire arrays (26, 27), will allow lateral mobility of the photogenerated charge carriers along the wire length, and thus will relax the mass transport limitations relative to those indicated by simulations, which assumed a constant flux of photogenerated charge carriers along the length of the wires in the array.

In conclusion, the physical integration of metal contacts into ordered microporous photoelectrodes provides an interesting opportunity to achieve optimized mass transport of reactants and products, as well as to minimize the ohmic potential drops due to the solution resistance in the cell. The metal contacts embedded at the base of the photoelectrodes also inherently served as an effective back-reflector that enhanced the optical absorption of the Si microwire array devices. In contact with a test electrolyte, PC–1.0 M $LiClO_4$–0.150 M $CoCp_2^+$–0.150 M $CoCp_2^0$, the integrated microwire photoelectrodes exhibited nearly ideal short-circuit current density in a stand-alone, two-terminal photoelectrochemical solar cell without any carrier collection loss due to the redox couple mass transport. The highly integrated microwire arrays, electrolyte, and embedded electrical contact system thus provides a promising device architecture for photosynthetic systems, such as solar-driven water-splitting photoelectrochemical cells.

Experimental Methods

Computational Modeling of Mass Transport in Wire-Array Structures. The 3-D diffusion equations of the wire-array geometries of interest were solved using the COMSOL Multiphysics finite-element-analysis software package, in conjunction with MATLAB. Three types of boundary conditions were applied in the numerical simulation. Symmetric boundary conditions were imposed for the four sidewalls of the simulation region. Dirichlet (or first-type) boundary conditions were employed at the hydrodynamic boundary layer, where the concentrations of the reduced and oxidized species, respectively, were equal to their concentrations in the bulk of the solution. For the Dirichlet boundary condition, beyond the hydrodynamic boundary layer thickness, Δ_0 (determined experimentally), convection was assumed to maintain uniform concentrations of both redox species at values that were equal to their bulk concentrations (also determined experimentally). Neumann (or second-type) boundary conditions were employed for the redox couple flux at the photoelectrode surface. For the Neumann boundary condition, a uniform current flux was assumed at the wire-array surface. For wire-array electrodes that had metal films at the bases of the wires, the Neumann boundary condition and the continuity equation were imposed at the base of the electrode, so that the inward cathodic flux was equal to the outward anodic flux. Other constants, including the geometries of the wires, as well as the diffusion coefficients and concentrations of the redox species, were set to the experimentally determined values.

The ohmic resistance loss in Scheme 1*C* was simulated by solving the 3D Poisson's equation in COMSOL Multiphysics. A periodic boundary condition was employed for the four sidewalls of the simulation region. The top of the simulation regions was assumed to be a perfect electrical insulator. Electrical ground was established at the metal counter electrode. The Neumann boundary condition for the uniform current flux was applied at the Si microwire electrode surface, where the current density at the electrode surface was normalized by the geometry factors such that the current density per unit of projected area was equal to 10 $mA\,cm^{-2}$. The conductivity of the electrolyte was set to a value of 5.0 $S\,m^{-1}$ in the subdomain settings.

Fabrication and Photoelectrochemical Evaluation of Wire Array Photoelectrodes. The p-Si wire arrays (*SI Text*) were formed into electrodes as described previously (13–15). Some wire-array samples were instead thermally oxidized at 1,100 °C under O_2 (4,000 sccm) for 90 min, followed by electron-beam evaporation of >500 nm Al_2O_3 (99.99%, Kurt Lesker) over the entire sample, and then by deposition of 200 nm of Ag. Ohmic contact was made by scratching the back side of the substrate with Ga:In eutectic. Contact to the interdigited Ag film that was located between the Si microwires, as well as to the side of the oxide-isolated substrate, was made by affixing a Cu/Sn wire to the Ag by use of silver solder (McMaster-Carr).

Two cell configurations, the control figuration and the device configuration, were evaluated in nonaqueous photoelectrochemical cells (*SI Text*) to compare the energy-conversion performance of the Si wire-array electrodes. In the control configuration (Scheme 2*A*), the Si wire-array electrode served as the working electrode, the Pt gauze electrode served as the counter electrode, and the Pt wire served as reference electrode. In the device configuration (Scheme 2*B*), the Si wire-array electrode served as the working electrode, the base Ag film served as the counter electrode, and the Pt wire served as the reference electrode.

J-E data were also evaluated in a stand-alone two-electrode configuration in which the Si wire-array electrode served as the photocathode and the bottom Ag film served as the counter electrode (Scheme 1*C*). In this configuration, a calibrated Si photodiode was placed next to the Si wire array electrode, and a droplet of solution that contained the $CoCp_2^{+/0}$ redox couple was used to make liquid contact to the electrodes.

ACKNOWLEDGMENTS. This work was supported by the U.S. Department of Energy, Grant DE-FG0203ER15483 and by the Caltech Center for Sustainable Energy Research (CCSER). One of us (A.C.M.) acknowledges support from Caltech's Summer Undergraduate Research Fellowship program.

1. Scharifker BR, Hills GJ (1981) Electrochemical kinetics at microscopically small electrodes. *J Electroanal Chem* 130:81–97.
2. Heerman L, Tarallo A (1999) Theory of the chronoamperometric transient for electrochemical nucleation with diffusion-controlled growth. *J Electroanal Chem* 470:70–76.
3. Scharifker BR, Mostany J (1984) 3-Dimensional nucleation with diffusion controlled growth 1: Number density of active-sites and nucleation rates per site. *J Electroanal Chem* 177:13–23.
4. Heerman L, Tarallo A (2000) Electrochemical nucleation with diffusion-limited growth. Properties and analysis of transients. *Electrochem Commun* 2:85–89.
5. Sluytersrehbach M, Wijenberg JHOJ, Bosco E, Sluyters JH (1987) The theory of chronoamperometry for the investigation of electrocrystallization—mathematical-description and analysis in the case of diffusion-controlled growth. *J Electroanal Chem* 236:1–20.
6. Penner RM, Heben MJ, Lewis NS (1989) Preparation and electrochemical characterization of conical and hemispherical ultramicroelectrodes. *Anal Chem* 61:1630–1636.
7. Kalaignan GP, Kang YS (2006) A review on mass transport in dye-sensitized nanocrystalline solar cells. *J Photochem Photobiol C* 7:17–22.
8. Lin Y, et al. (2006) Computer simulations of light scattering and mass transport of dye-sensitized nanocrystalline solar cells. *J Electroanal Chem* 588:51–58.
9. Hyk W, Augustynski J (2006) Steady-state operation of porous photoelectrochemical cells under the conditions of mixed diffusional and migrational mass transport—Theory. *J Electrochem Soc* 153:A2326–A2341.
10. Papageorgiou N, Gratzel M, Infelta PP (1996) On the relevance of mass transport in thin layer nanocrystalline photoelectrochemical solar cells. *Sol Energy Mater Sol Cells* 44:405–438.
11. Lee JJ, Coia GM, Lewis NS (2004) Current density versus potential characteristics of dye-sensitized nanostructured semiconductor photoelectrodes. 1. Analytical expressions. *J Phys Chem B* 108:5269–5281.
12. Lee JJ, Coia GM, Lewis NS (2004) Current density versus potential characteristics of dye-sensitized nanostructured semiconductor photoelectrodes. 2. Simulations. *J Phys Chem B* 108:5282–5293.
13. Boettcher SW, et al. (2010) Energy-conversion properties of vapor-liquid-solid-grown silicon wire-array photocathodes. *Science* 327:185–187.
14. Maiolo JR, Atwater HA, Lewis NS (2008) Macroporous silicon as a model for silicon wire array solar cells. *J Phys Chem C* 112:6194–6201.
15. Maiolo JR, et al. (2007) High aspect ratio silicon wire array photoelectrochemical cells. *J Am Chem Soc* 129:12346–12353.
16. Garnett E, Yang PD (2010) Light trapping in silicon nanowire solar cells. *Nano Lett* 10:1082–1087.
17. Yuhas BD, Yang PD (2009) Nanowire-based all-oxide solar cells. *J Am Chem Soc* 131:3756–3761.
18. Garnett EC, Yang PD (2008) Silicon nanowire radial p-n junction solar cells. *J Am Chem Soc* 130:9224–9227.
19. Kayes BM, Atwater HA, Lewis NS (2005) Comparison of the device physics principles of planar and radial p-n junction nanorod solar cells. *J Appl Phys* 97:114302.
20. Bard AJ, Faulkner LR (2000) *Electrochemical Methods, Fundamentals and Applications* (Wiley, New York), 2nd Ed.
21. Gibbons JF, Cogan GW, Gronet CM, Lewis NS (1984) A 14-percent efficient nonaqueous semiconductor liquid junction solar-cell. *Appl Phys Lett* 45:1095–1097.
22. Gratzel M (2001) Photoelectrochemical cells. *Nature* 414:338–344.
23. Parkinson B (1982) An evaluation of various configurations for photo-electrochemical photo-voltaic solar-cells. *Sol Cells* 6:177–189.
24. Fajardo AM, Lewis NS (1997) Free-energy dependence of electron-transfer rate constants at Si/liquid interfaces. *J Phys Chem B* 101:11136–11151.
25. Kelzenberg MD, et al. (2010) Enhanced absorption and carrier collection in Si wire arrays for photovoltaic applications. *Nat Mater* 9:239–244.
26. Boettcher SW, et al. (2011) Photoelectrochemical hydrogen evolution using Si microwire arrays. *J Am Chem Soc* 133:1216–1219.
27. Kelzenberg MD, et al. (2011) High-performance Si microwire photovoltaics. *Energ Environ Sci* 4:866–871.
28. Putnam MC, et al. (2010) Si microwire-array solar cells. *Energ Environ Sci* 3:1037–1041.
29. Tan MX, et al. (1994) Principles and applications of semiconductor photoelectrochemistry. *Prog Inorg Chem* 41:21–144.
30. Kelzenberg MD, Putnam MC, Turner-Evans DB, Lewis NS, Atwater HA (2009) Predicted efficiency of Si wire array solar cells. *Proceedings of the 34th IEEE PVSC* pp 391–396.